Photo-thermoelectric effect-driven detection of optical communication light in graphene/hBN heterostructures

Takuya Iwasaki[1]*, Yodai Sato[2], Makoto Ogo[2], Byunghun Oh[2], Daichi Kozawa[1], Ryo Kitaura[1], Kenji Watanabe[3], Takashi Taniguchi[1], Satoshi Moriyama[2], and Junichi Fujikata[4]

[1]*Research Center for Materials Nanoarchitectonics, National Institute for Materials Science, Tsukuba, Ibaraki 305-0044, Japan*

[2]*Department of Electrical and Electronic Engineering, Tokyo Denki University, Adachi, Tokyo 120-8551, Japan*

[3]*Research Center for Electronic and Optical Materials, National Institute for Materials Science, Tsukuba, Ibaraki 305-0044, Japan*

[4]*Institute of Post-LED Photonics, Tokushima University, 2-1, Minami-Josanjima, Tokushima 770-8506, Japan*

We report on the photodetection properties of high-quality graphene encapsulated by hexagonal boron nitride under illumination with optical communication light. We demonstrate a gate-tunable photocurrent and zero-bias switching cycle operation at room temperature. Through gate- and temperature-dependent photocurrent measurements, we determine that the dominant photoresponse mechanism is the photo-thermoelectric effect. At low temperatures, the photocurrent in finite doping regions correlates with the Seebeck coefficient, while sharp peaks emerge near the charge neutrality point due to an edge-excited photocurrent. Our study provides guidelines for high-performance graphene-based optoelectronic devices.

Graphene has garnered attention due to its excellent electronic and optical properties, such as a broad light absorption range, high conductivity, and high carrier mobility.[1)] Owing to its ultrafast photo-excitation dynamics, graphene is particularly anticipated as a building block for high-speed optoelectronic devices in fiber-optic communication bands from 1260 to 1625 nm. Studies have explored photodetection at the low-loss wavelength of 1550 nm using graphene on SiO_2,[2–5)] carbon nanotubes,[6)] Si waveguides (WGs),[7–14)] SiN WGs,[15,16)] plasmonic cavities,[17)] and metamaterials.[18)] A high responsivity of ~50 mA/W was demonstrated in graphene/Si WG-integrated devices,[9)] and graphene-metamaterial hybrid devices demonstrated an ultrafast operating speed of >500 GHz.[18)]

Despite such high performance, the quality of graphene in previous studies was limited due to the use of chemical vapor deposition-grown graphene[6,10,14–18)] and/or gate dielectrics, which could degrade the quality of the product.[14–16)] To enhance graphene photodetector

*E-mail: IWASAKI.Takuya@nims.ac.jp

performance, improving its electronic quality (e.g., carrier mobility) is crucial. Encapsulation of exfoliated graphene with hexagonal boron nitride (hBN), forming a hBN/graphene/hBN heterostructure, is a promising approach.[19] A previous study using hBN/graphene/hBN heterostructures on Si WGs demonstrated high-speed operation and high responsivity; however, the low carrier mobility of 1000 $cm^2/V{\cdot}s$, below that of typical graphene devices, might have limited performance.[11] Recent time-resolved measurements have demonstrated that the operating speed of high-quality graphene devices based on hBN/graphene/hBN heterostructures reaches 220 GHz for visible light excitation.[20] Accordingly, a hBN/graphene/hBN heterostructure is key to achieving high-performance photodetectors. Investigating photodetection characteristics for optical communication bands in high-quality hBN/graphene/hBN devices is imperative; however, this area has received limited exploration. In particular, a device consisting of hBN/graphene/hBN heterostructures on SiO_2/Si substrates, a typical high-quality graphene device structure, has not been adopted so far.

Furthermore, understanding the photoresponse mechanism is crucial for improving photodetector performance. Although the photoresponse mechanism varies with device design and materials, an intrinsic photodetection mechanism in graphene is hypothesized to be a photo-thermoelectric (PTE) effect,[21,22] generating a photoresponse through a temperature gradient and the thermoelectric (Seebeck) effect. This gradient is caused by the ultrafast cooling of photo-excited-hot carriers in graphene.[23–25] As the PTE-induced photoresponse emerges without an external bias voltage,[14–16,18,21,22] it enables zero-bias and zero-dark current operation, leading to low noise and low power consumption in device applications.

In this study, we investigate the photodetection properties of the hBN/graphene/hBN device on a typical SiO_2/Si substrate under simple top illumination at a wavelength of 1550 nm. We examine the gate- and temperature-dependence of the photoresponse in our device to elucidate the photoresponse mechanism in hBN/graphene/hBN heterostructures. Our results suggest that the dominant mechanism of the photocurrent generation is the PTE effect, allowing the gate-tunable zero-bias photoresponse.

For device fabrication, single-layer graphene (SLG) and hBN flakes were prepared on a 90-nm SiO_2/Si substrate through mechanical exfoliation from bulk crystals. The hBN/SLG/hBN heterostructure was assembled via a modified dry transfer method as described in [26] . Electron-beam (EB) lithography and reactive ion etching (SF_6 plasma) were employed to selectively etch the top hBN layer to expose the contact region, ensuring SLG was not etched due to fluorination of its surface.[27] Subsequently, contact electrodes (Cr/Pd/Au) were deposited directly over the EB resist, followed by liftoff. The schematic cross-section and optical image of the fabricated

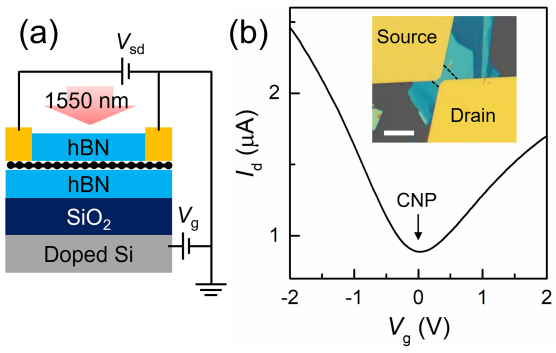

Fig. 1. (a) Schematic cross-section of our device. (b) Drain current as a function of V_g at V_{sd} = 1 mV, T = 300 K in the dark. The inset exhibits the optical image of our device. The represented scale bar is 10 μm. The dotted lines represent the edge of graphene.

device are displayed in Fig. 1(a) and the inset of Fig. 1(b), respectively. Measurements were conducted in a vacuum using a helium optical cryostat, allowing temperature (T) control down to 8 K. A two-terminal DC drain current (I_d) of the device was measured by applying a source-drain bias voltage (V_{sd}) using a source-measure unit. A highly doped Si substrate served as a back gate to adjust the Fermi energy of graphene. The device was illuminated using a semiconductor laser at a wavelength of 1550 nm and a spot diameter of ~4.5 μm. Given that the laser spot size exceeds that of the graphene channel, we referred to the laser power as the internal power (P_{in}) at the device.

Initially, we examine the standard transport property of our device at room temperature. Figure 1(b) illustrates the drain current as a function of the back-gate voltage (V_g) at T = 300 K, indicating typical ambipolar behavior with the charge neutrality point (CNP) located at $V_g \sim 0$ V. This behavior suggests minimal external doping in the graphene due to hBN encapsulation. The field-effect mobility is estimated by $\mu_{FE} = (dI_d/dV_g)L/(WV_{sd}C_g)$, where L is the channel length, W is the channel width, C_g is the gate capacitance per unit area. We obtain $\mu_{FE} \sim 9600$ cm^2/V·s for electrons and $\mu_{FE} \sim 19000$ cm^2/V·s for holes, higher than that in typical graphene on SiO_2 and WG-integrated graphene devices.[11–16)]

Next, we explore the photoresponse in our device. Figure 2(a) displays the transient photoresponse characteristics at zero-bias voltage ($V_{sd} \sim 0$). We monitor the change in I_d when turning on and off the light illumination. At V_g = 1 V, a finite photoresponse is observed, as presented in the top panel of Fig. 2(a). Conversely, a negative photoresponse at $V_g = -1$ V is also observed, as depicted in the bottom panel of Fig. 2(a). These results indicate that the sign and intensity of the photoresponse depend on V_g, and our device operates at zero bias. The on/off tracing speed is instantaneous on a 10-ms timescale (the inset of Fig. 2(a)), limited

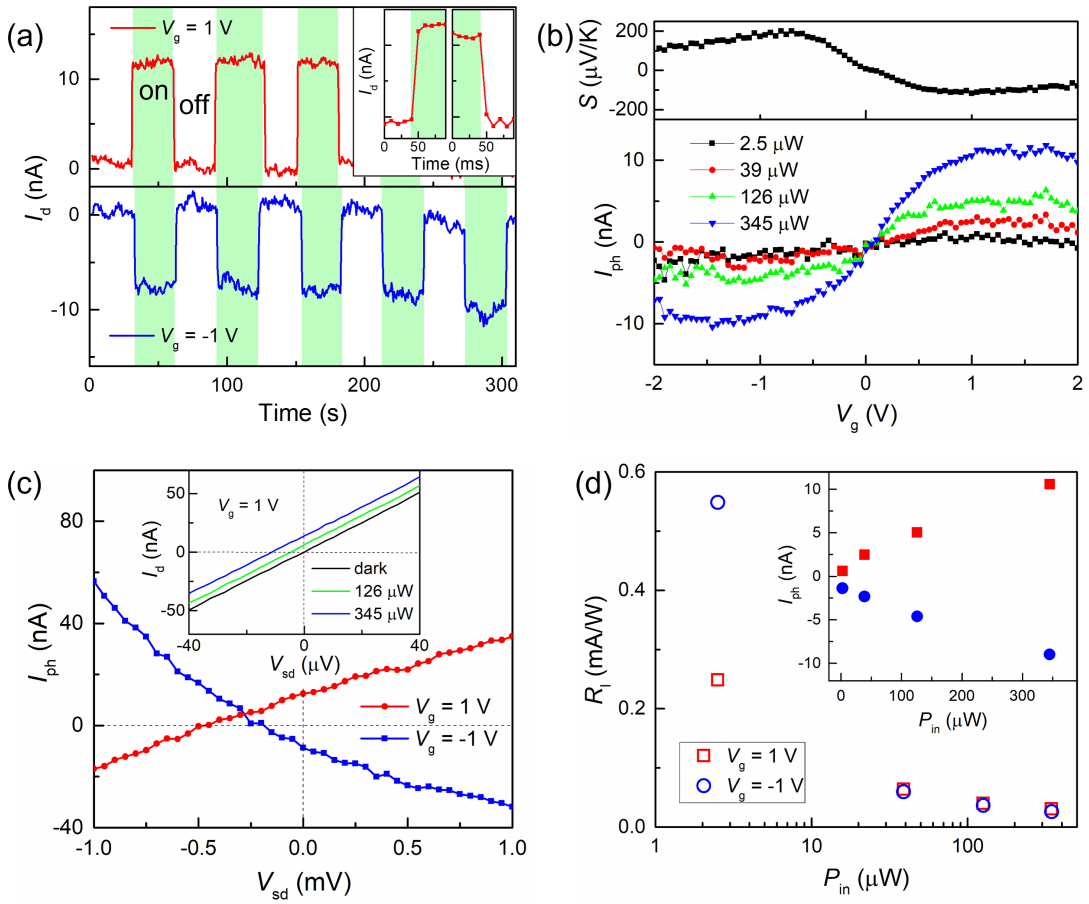

Fig. 2. Photodetection at T = 300 K. (a) Zero-bias switching cycles at V_g = 1 V (top), −1 V (bottom) with P_{in} = 345 μW. The inset shows the photoresponse at illumination switching. The green-shaded region represents the data from the device under illumination. (b) Seebeck coefficient (top) and zero-bias photocurrent (bottom) as a function of V_g and P_{in}. (c) Bias voltage dependence of the photocurrent with P_{in} = 345 μW. The inset exhibits the I_d-V_{sd} curves in the dark and under illumination at V_g = 1 V. (d) Responsivity and photocurrent (inset) as a function of P_{in} at zero bias.

by our measurement system.

Investigating the gate-dependence of the photocurrent provides insight into the photoresponse mechanism. Here, the photocurrent (I_{ph}) is defined as the difference between the drain current under illumination (I_{light}) and in the dark (I_{dark}), i.e., $I_{ph} = I_{light} - I_{dark}$. The bottom panel of Fig. 2(b) exhibits the dependence of I_{ph} on V_g at zero bias ($I_{dark} \sim 0$). The sign of I_{ph} switches upon crossing the CNP, whereas the photocurrent vanishes at the CNP. In other words, the photocurrent is negative (positive) when the Fermi energy lies in the valence (conduction) band. This feature can be attributed to the PTE effect,[22] and is discussed below.

The sign reversal of I_{ph} across the CNP could reflect the dependence of the Seebeck

coefficient (S) on the carrier density.[21,22,28,29] The Seebeck coefficient, which converts a temperature gradient into a built-in voltage, can be derived from the transport characteristics by the modified Mott formula:[21,22,28,30]

$$S = -\frac{\pi^2 k_B^2 T}{3eG}\frac{dG}{dV_g}\frac{dV_g}{dE}\bigg|_{E=E_F} \tag{1}$$

where k_B is the Boltzmann constant, e is the elementary charge, $G(= I_d/V_{sd})$ is the electrical conductance, and E_F is the Fermi energy. Using the Fermi energy of SLG, $E_F = \hbar v_F\sqrt{\pi n}$ ($\hbar$ is the Planck constant divided by 2π, $v_F \sim 10^6$ m/s is the Fermi velocity of graphene[31]) and the carrier density, $n = C_g(V_g - V_{CNP})/e$ (V_{CNP} is the gate voltage at the CNP), we calculate the Seebeck coefficient as shown in the top panel of Fig. 2(b). The absolute value of S increases as doping deceases, reaching a maximum value of ~200 μV/K, in good agreement with values from the literature for high-quality graphene/hBN devices.[29] Upon further decreasing the doping, the S value decreases and vanishes at the CNP. This is due to the opposite contribution of electrons and holes near the CNP to S. Consequently, the sign of S switches at the CNP, analogous to the dependence of I_{ph} on V_g in our device.

In our configuration, although the graphene channel is smaller than the laser spot, it is possible that one of the two graphene-electrode interfaces heats up significantly due to deviation in the center location of the laser spot. Additionally, the graphene channel away from the electrodes is n-doped (p-doped) for $V_g > V_{CNP}(< V_{CNP})$, while the chemical potential near the graphene-electrode interface is pinned by the doping from the metal electrode.[32] Consequently, an n-i (p-i) interface forms in the graphene channel, where regions with different S connect. This creates a temperature gradient and induces the PTE effect in our device.

To analyze the PTE effect, we calculate the temperature difference resulting in the photoresponse using $\Delta T_{PTE} = V_{ph}/\Delta S$, where $V_{ph}(= I_{ph}R)$ is the PTE-induced photovoltage and $R(= G^{-1})$ is the resistance. Considering $R \sim 780$ Ω and $\Delta S \sim 117$ μV/K at $V_g = 1$ V, and $P_{in} = 345$ μW, we obtain $\Delta T_{PTE} \sim 0.1$ K. Furthermore, we estimate the temperature increase induced by illumination (ΔT) by considering heat flow as a plane-wavefront; $\Delta T = (L/2t_{gr}W)(P_{in}\alpha/\kappa)$,[21,33] where t_{gr} is the thickness, $\alpha = 2.3\%$ is the absorption coefficient, and κ ~5300 W/m·K is the thermal conductivity of SLG.[33] This calculation yields $\Delta T \sim$ 0.6 K, in the same order of magnitude and consistent with ΔT_{PTE}. It is noted that illumination of both source and drain electrodes could reduce net photocurrent due to the cancellation of symmetric photocurrents from opposite-directional graphene-electrode interfaces,[22,34,35] potentially leading to an underestimation of ΔT_{PTE}. From this analysis, we deduce that the PTE effect predominates in the photoresponse mechanism of our device.

It should be considered that there are other potential mechanisms for photocurrent generation, such as photovoltaic, bolometric, and photogating effects. However, if the photovoltaic effect was dominant, a sign switch of I_{ph} would not occur upon crossing the CNP.[3,18] The bolometric effect requires a bias voltage to observe a photocurrent,[36] contrary to the zero-bias photoresponse in our device. The photogating effect is unlikely in our device because graphene is isolated from potential charge traps by the hBN encapsulation.[6,37] Moreover, photogating effects from a doped Si substrate should not occur for wavelengths >1100 nm, as the excitation energy is lower than the bandgap of Si.[37]

We reaffirm the zero-bias photoresponse in the I_{ph}-V_{sd} and I_d-V_{sd} characteristics depicted in Fig. 2(c) and its inset, respectively. For V_g = 1 V (−1 V), the photocurrent increases (decreases) with increasing V_{sd}, becoming zero at $V_{sd} \sim -0.45$ mV (−0.2 mV). This reflects the polarity of the photovoltage, where the bias voltage enhances (cancels out) the photovoltage when its polarity is the same (opposite). At finite V_{sd}, the photoconductive effect might also contribute to enhancing I_{ph}.

The figure-of-merit values are instrumental in evaluating the photodetector performance of our device. As shown in the bottom panel of Fig. 2(b) and the inset of Fig. 2(d), the absolute values of I_{ph} increase with P_{in}. The maximum responsivity $R_I (= I_{ph}/P_{in})$ is ∼0.55 mA/W at zero bias (Fig. 2(d)). Assuming the noise current originates from the thermal Johnson-Nyquist contribution,[38] we estimate the minimum noise equivalent power (NEP = $\sqrt{4k_BT/R}/R_I$) to be ∼9.5 nW/Hz$^{-1/2}$. These values are comparable to conventional graphene photodetectors (zero bias, 1550-nm top illumination).[2,3,11] It should be noted that the PTE-induced photocurrent is dependent on the laser spot position and is enhanced when the laser is focused on a graphene-electrode interface. Thus, the device performance could be improved by enlarging the graphene channel size, introducing the asymmetric geometry, and focusing on one side of the graphene-electrode interfaces.

We then consider the low-temperature characteristics and temperature dependence of the photoresponse. Figure 3(a) and its inset display the I_d-V_g and I_d-V_{sd} characteristics at T = 20 K, respectively. At low T, the CNP shifts slightly to $V_g \sim -0.4$ V. We confirm Ohmic contact through the linearity of I_d-V_{sd} curves across all T ranges in this study (20−300 K), thus ruling out the possibility of photocurrent generation due to a Schottky contact. In contrast to the I_{ph}-V_g curves at T = 300 K, we observe two distinct I_{ph} peaks at T = 20 K as presented in Fig. 3(b). One peak is positive at the CNP ("CNP peak"), while the other is negative at a slightly positive V_g from the CNP ("negative peak"). The maximum absolute values of these peaks increase with increasing P_{in}.

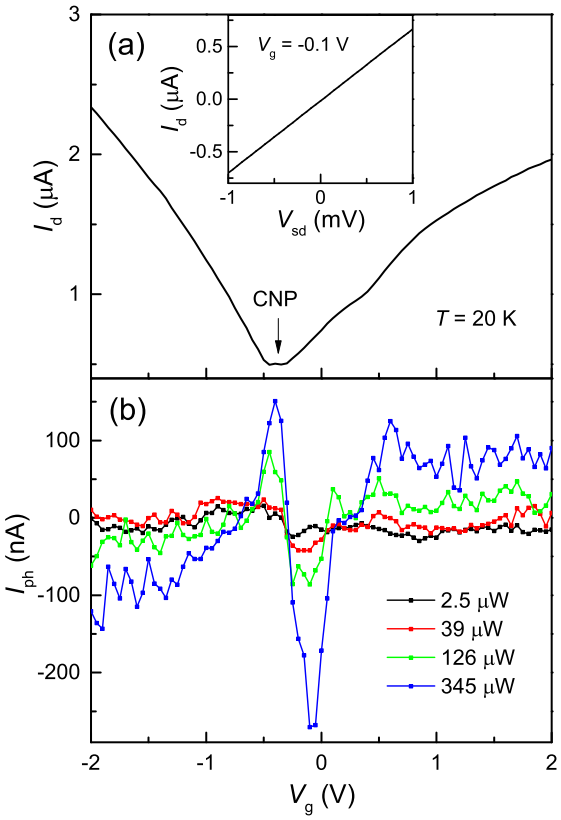

Fig. 3. (a) Drain current vs V_g at V_{sd} = 1 mV, T = 20 K in the dark. The inset exhibits the I_d-V_{sd} curve at V_g = −0.1 V. (b) Photocurrent as a function of V_g and P_{in} at T = 20 K.

To determine whether the peaks originate from the PTE effect, we calculate the Seebeck coefficient using Eq. 1 for various T (Fig. 4(a)). As T decreases, the $|S|$ value diminishes, and the V_g positions of maximum positive and negative S shift toward the CNP. This shift corresponds to the narrowing of the energy region dominated by electron-hole puddles, a result of reduced thermal excitation of electrons and holes at lower T.[29] As illustrated in Fig. 4(b), the $|I_{ph}|$ values also decrease with T in the finite doping regions. It is noteworthy that at T = 20 K, the photocurrent exhibits strong fluctuations due to the influence of the I_{ph} peaks. By tracking the maximum positive S (S_{max}) and I_{ph} values at the same V_g position across various T, we observe their correlated temperature dependence, as depicted in the inset of Fig. 4(a). This correlation indicates that the photocurrent is dependent on S, supporting the dominance of the PTE effect in the photoresponse mechanism for finite doping regions. However, the positions of the I_{ph} peaks do not depend on either T nor S. As T increases, the intensity of I_{ph} peaks diminishes, and they disappear for $T \geq 200$ K (Fig. 4(b)). These observations suggest that the mechanism behind the I_{ph} peaks differs from the PTE effect.

The device geometry and the size of the laser spot suggest that an edge-excited photocurrent

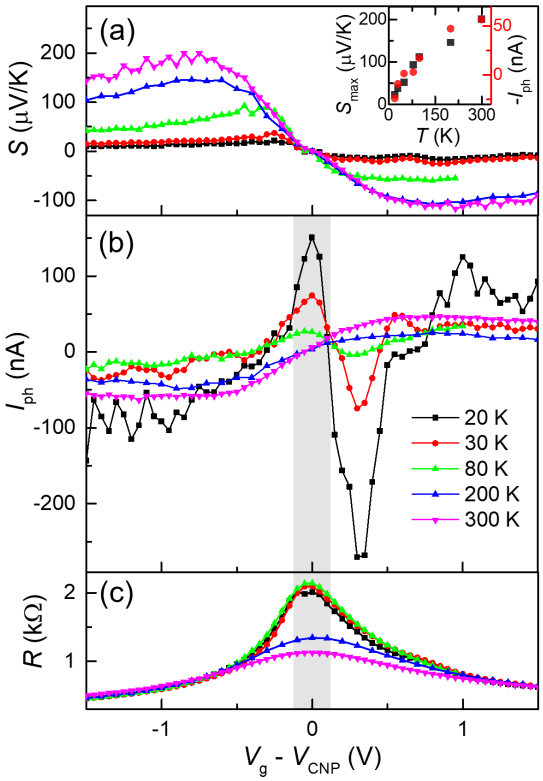

Fig. 4. (a-c) Temperature and back-gate voltage dependence of the (a) S, (b) I_{ph} at V_{sd} = 1 mV, and (c) R. The CNP peak region is shaded in (b,c). The inset of (a) presents the T dependence of S_{max} and I_{ph}.

(EPC) might explain the CNP peak.[35] The EPC arises from potential symmetry breaking at graphene edges and strong electron-electron interaction in charge-neutral graphene. In our case, the illumination with a laser spot covering the graphene edges could lead to the generation of the EPC. As the EPC is sensitive to the charge-neutral state of graphene, the width of the CNP peak should be narrower than that of the resistance peak.[35] This characteristic is observable in our device, as indicated by the shaded region in Figs. 4(b) and (c).

Conversely, the negative peak, not observed in previous studies, presents a unique case. Depending on the channel symmetry, the EPC mights assume a negative value but would typically appear at the CNP.[35] Therefore, neither the PTE effect nor edge excitation can fully explain the negative peak. A plausible cause for the emergence of the negative peak could be the photogating effect from charge traps, activated at low T, due to impurities at the graphene/hBN or hBN/SiO_2 interfaces. However, the precise origin of the negative peak and the reason for the disappearance of the CNP peak at high temperatures remain unclear and are subjects for further investigation.

In summary, we have fabricated an hBN/graphene/hBN device and investigated its pho-

todetection characteristics for optical communication light. Our analysis of the gate- and temperature-dependent photoresponse in this device reveals that the predominant photodetection mechanism is the PTE effect. The ability to tune the photoresponse via the gate voltage enables the ambipolar zero-bias switching operations at room temperature. To deepen understanding of the PTE effect and contribution of other photoresponse mechanisms, investigating local photoresponse by photocurrent mapping on a graphene channel larger than a laser spot is left as a future task. Since the photoresponse could result from the asymmetricity of the device, the device performance could be improved by introducing asymmetric factors such as channel and electrode structures. It is noteworthy that a simple structure on a typical SiO_2/Si substrate was utilized in this study. This structure offers the potential for additional functionalities. For instance, integrating local gates into this setup could allow for the electrostatic definition of pn junctions within in a graphene channel, leading to highly responsive photodetectors without compromising the carrier mobility of graphene. Our study provides the fundamental insight into the photodetection properties of hBN/graphene/hBN heterostructure devices. Regarding the role of hBN in addition to improving the quality of graphene, out-of-plane energy transfer, due to the coupling between charge carriers in graphene and hyperbolic phonon polaritons in hBN, may influence the photoexcitation/hot carrier relaxation process.[39,40] This suggests that designing proper geometrical parameters, such as the thickness of hBN and the graphene channel size, could enhance the PTE effect. Given their high carrier mobility and Seebeck coefficient, hBN/graphene/hBN heterostructures hold promise as the foundation for future high-performance optoelectronic devices.

Acknowledgment

This work was partially supported by JPSJ KAKENHI Grant No. 21H01400, 21H01749, 22H01555, 22H01893, 23H00274, 23H05469 and the Advanced Research Infrastructure for Materials and Nanotechnology in Japan (ARIM) of the Ministry of Education, Culture, Sports, Science and Technology (MEXT). Proposal Number JPMXP1223NM5186.

References

1) M. Romagnoli, V. Sorianello, M. Midrio, F. H. L. Koppens, C. Huyghebaert, D. Neumaier, P. Galli, W. Templ, A. D'Errico, and A. C. Ferrari, Nat. Rev. Mater. **3**, 392 (2018).
2) F. Xia, T. Mueller, Y. Lin, A. Valdes-Garcia, and P. Avouris, Nat. Nanotechnol. **4**, 839 (2009).
3) T. Mueller, F. Xia, and P. Avouris, Nat. Photon. **4**, 297 (2010).
4) A. Urich, K. Unterrainer, and T. Mueller, Nano Lett. **11**, 2804 (2011).
5) T. J. Echtermeyer, P. S. Nene, M. Trushin, R. V. Gorbachev, A. L. Eiden, S. Milana, Z. Sun, J. Schliemann, E. Lidorikis, K. S. Novoselov, and A. C. Ferrari, Nano Lett. **14**, 3733 (2014).
6) Y. Liu, F. Wang, X. Wang, X. Wang, E. Flahaut, X. Liu, Y. Li, X. Wang, Y. Xu, Y. Shi, and R. Zhang, Nat. Commun. **6**, 8589 (2015).
7) X. Gan, R.-J. Shiue, Y. Gao, I. Meric, T. F. Heinz, K. Shepard, J. Hone, S. Assefa, and D. Englund, Nat. Photon. **7**, 883 (2013).
8) X. Wang, Z. Cheng, K. Xu, H. K. Tsang, and J.-B. Xu, Nat. Photon. **7**, 888 (2013).
9) A. Pospischil, M. Humer, M. M. Furchi, D. Bachmann, R. Guider, T. Fromherz, and T. Mueller, Nat. Photon. **7**, 892 (2013).
10) D. Schall, D. Neumaier, M. Mohsin, B. Chmielak, J. Bolten, C. Porschatis, A. Prinzen, C. Matheisen, W. Kuebart, B. Junginger, W. Templ, A. L. Giesecke, and H. Kurz, ACS Photonics **1**, 781 (2014).
11) R.-J. Shiue, Y. Gao, Y. Wang, C. Peng, A. D. Robertson, D. K. Efetov, S. Assefa, F. H. L. Koppens, J. Hone, and D. Englund, Nano Lett. **15**, 7288 (2015).
12) S. Schuler, D. Schall, D. Neumaier, L. Dobusch, O. Bethge, B. Schwarz, M. Krall, and T. Mueller, Nano Lett. **16**, 7107 (2016).
13) S. Schuler, D. Schall, D. Neumaier, B. Schwarz, K. Watanabe, T. Taniguchi, and T. Mueller, ACS Photonics **5**, 4758 (2018).
14) S. Marconi, M. A. Giambra, A. Montanaro, V. Mišeikis, S. Soresi, S. Tirelli, P. Galli, F. Buchali, W. Templ, C. Coletti, V. Sorianello, M. Romagnoli, Nat. Commun. **12**, 806 (2021).
15) J. E. Muench, A. Ruocco, M. A. Giambra, V. Miseikis, D. Zhang, J. Wang, H. F. Y. Watson, G. C. Park, S. Akhavan, V. Sorianello, M. Midrio, A. Tomadin, C. Coletti, M. Romagnoli, A. C. Ferrari, and I. Goykhman, Nano Lett. **19**, 7632 (2019).

16) V. Mišeikis, S. Marconi, M. A. Giambra, A. Montanaro, L. Martini, F. Fabbri, S. Pezzini, G. Piccinini, S. Forti, B. Terrés, I. Goykhman, L. Hamidouche, P. Legagneux, V. Sorianello, A. C. Ferrari, F. H. L. Koppens, M. Romagnoli, and C. Coletti, ACS Nano **14**, 11190 (2020).

17) Z. Chen, X. Li, J. Wang, L. Tao, M. Long, S.-J. Liang, L. K. Ang, C. Shu, H. Ki Tsang, and J.-B. Xu, ACS Nano **11**, 430 (2017).

18) S. M. Koepfli, M. Baumann, Y. Koyaz, R. Gadola, A. Güngör, K. Keller, Y. Horst, S. Nashashibi, R. Schwanninger, M. Doderer, E. Passerini, Y. Fedoryshyn, and J. Leuthold, Science **380**, 1169 (2023).

19) C. R. Dean, A. F. Young, I. Meric, C. Lee, L. Wang, S. Sorgenfrei, K. Watanabe, T. Taniguchi, P. Kim, K. L. Shepard, and J. Hone, Nat. Nanotechnol. **5**, 722 (2010).

20) K. Yoshioka, T. Wakamura, M. Hashisaka, K. Watanabe, T. Taniguchi, and N. Kumada, Nat. Photon. **16**, 718 (2022).

21) X. Xu, N. M. Gabor, J. S. Alden, A. M. van der Zande, and P. L. McEuen, Nano Lett. **10**, 562 (2010).

22) N. M. Gabor, J. C. W. Song, Q. Ma, N. L. Nair, T. Taychatanapat, K. Watanabe, T. Taniguchi, L. S. Levitov, and P. Jarillo-Herrero, Science **334**, 648 (2011).

23) K. J. Tielrooij, J. C. W. Song, S. A. Jensen, A. Centeno, A. Pesquera, A. Zurutuza Elorza, M. Bonn, L. S. Levitov, and F. H. L. Koppens, Nat. Phys. **9**, 248 (2013).

24) R. Bistritzer and A. H. MacDonald, Phys. Rev. Lett. **102**, 206410 (2009).

25) A. Tomadin, S. M. Hornett, H. I. Wang, E. M. Alexeev, A. Candini, C. Coletti, D. Turchinovich, M. Kläui, M. Bonn, F. H. L. Koppens, E. Hendry, M. Polini, and K.-J. Tielrooij, Sci. Adv. **4**, eaar5313 (2018).

26) T. Iwasaki, K. Endo, E. Watanabe, D. Tsuya, Y. Morita, S. Nakaharai, Y. Noguchi, Y. Wakayama, K. Watanabe, T. Taniguchi, and S. Moriyama, ACS Appl. Mater. Interfaces **12**, 8533 (2020).

27) B. S. Jessen, L. Gammelgaard, M. R. Thomsen, D. M. A. Mackenzie, J. D. Thomsen, J. M. Caridad, E. Duegaard, K. Watanabe, T. Taniguchi, T. J. Booth, T. G. Pedersen, A.-P. Jauho, and P. Bøggild, Nat. Nanotechnol.**14**, 340 (2019).

28) Y. M. Zuev, W. Chang, and P. Kim, Phys. Rev. Lett. **102**, 096807 (2009).

29) J. Duan, X. Wang, X. Lai, G. Li, K. Watanabe, T. Taniguchi, M. Zebarjadi, and E. Y. Andrei, Proc. Natl. Acad. Sci. USA **113**, 14272 (2016).

30) M. Cutler and N. F. Mott, Phys. Rev. **181**, 1336 (1969).

31) S. Das Sarma, S. Adam, E. H. Hwang, and E. Rossi, Rev. Mod. Phys. **83**, 407 (2011).

32) T. Mueller, F. Xia, M. Freitag, J. Tsang, and P. Avouris, Phys. Rev. B **79**, 245130 (2009).
33) A. A. Balandin, S. Ghosh, W. Bao, I. Calizo, D. Teweldebrhan, F. Miao, and C. N. Lau, Nano Lett. **8**, 902 (2008).
34) F. Xia, T. Mueller, R. Golizadeh-Mojarad, M. Freitag, Y.-M. Lin, J. Tsang, V. Perebeinos, and P. Avouris, Nano Lett. **9**, 1039 (2009).
35) Q. Ma, C. H. Lui, J. C. W. Song, Y. Lin, J. F. Kong, Y. Cao, T. H. Dinh, N. L. Nair, W. Fang, K. Watanabe, T. Taniguchi, S.-Y. Xu, J. Kong, T. Palacios, N. Gedik, N. M. Gabor, and P. Jarillo-Herrero, Nat. Nanotechnol. **14**, 145 (2019).
36) J. Yan, M-H. Kim, J. A. Elle, A. B. Sushkov, G. S. Jenkins, H. M. Milchberg, M. S. Fuhrer, and H. D. Drew, Nat. Nanotechnol. **7**, 472 (2012).
37) F. Luo, M. Zhu, Y. Tan, H. Sun, W. Luo, G. Peng, Z. Zhu, X.-A. Zhang, and S. Qin, AIP Adv. **8**, 115106 (2018).
38) S. Castilla, B. Terrés, M. Autore, L. Viti, J. Li, A. Y. Nikitin, I. Vangelidis, K. Watanabe, T. Taniguchi, E. Lidorikis, M. S. Vitiello, R. Hillenbrand, K.-J. Tielrooij, and F. H. L. Koppens, Nano Lett. **19**, 2765 (2019).
39) K.-J. Tielrooij, N. C. H. Hesp, A. Principi, M. B. Lundeberg, E. A. A. Pogna, L. Banszerus, Z. Mics, M. Massicotte, P. Schmidt, D. Davydovskaya, D. G. Purdie, I. Goykhman, G. Soavi, A. Lombardo, K. Watanabe, T. Taniguchi, M. Bonn, D. Turchinovich, C. Stampfer, A. C. Ferrari, G. Cerullo, M. Polini, and F. H. L. Koppens, Nat. Nanotechnol. **3**, 41 (2018).
40) A. Woessner, R. Parret, D. Davydovskaya, Y. Gao, J.-S. Wu, M. B. Lundeberg, S. Nanot, P. Alonso-González, K. Watanabe, T. Taniguchi, R. Hillenbrand, M. M. Fogler, J. Hone, and F. H. L. Koppens, npj 2D Mater. Appl. **1**, 25 (2017).